Letter

Toward high-resolution low-energy electron spectroscopy with transition-edge sensors

R. Ammendola,[1] A. Apponi,[2] G. Benato,[3,4] M. G. Betti,[5,6] R. Biondi,[3,4] P. Bos,[7,8] M. Cadeddu,[9] A. Casale,[10] O. Castellano,[2,11] G. Cavoto,[5,6] L. Cecchini,[5] E. Celasco,[12,13] M. Chirico,[5,6] W. Chung,[14] A. G. Cocco,[3] A. P. Colijn,[7,8] B. Corcione,[5,6,*] N. D'Ambrosio,[3] M. D'Incecco,[3] G. De Bellis,[5,15] M. De Deo,[3] N. de Groot,[16] A. Esposito,[5,6] M. Farino,[14] S. Farinon,[12] A. D. Ferella,[3,17] L. Ferro,[9,18] L. Ficcadenti,[5] G. Galbato Muscio,[5,19] S. Gariazzo,[20,21,22] H. Garrone,[20,23,24] F. Gatti,[12,13] F. Malnati,[20,23,25] G. Mangano,[26,27] L. E. Marcucci,[28,29] C. Mariani,[5,6] J. Mead,[7,8] G. Menichetti,[29] M. Messina,[3] E. Monticone,[20,23] M. Naafs,[7] S. Nagorny,[3,4] V. Narcisi,[1,30] F. Pandolfi,[5] R. Pavarani,[9,18] C. Pepe,[23,31] C. Pérez de los Heros,[32] O. Pisanti,[26,27] F. M. Pofi,[3,4] A. D. Polosa,[5,6] I. Rago,[5] M. Rajteri,[20,23] S. Ritarossi,[2,11] N. Rossi,[3] A. Ruocco,[2,11] G. Salina,[1] A. Santucci,[9,18] M. Sestu,[9,18] A. Tan,[14] V. Tozzini,[28,33] C. G. Tully,[14] I. van Rens,[16] F. Virzi,[3,17] G. Visser,[7] and M. Viviani[28]

(PTOLEMY Collaboration)

[1]*INFN Sezione di Roma Tor Vergata, Roma, Italy*
[2]*INFN Sezione di Roma Tre, Roma, Italy*
[3]*INFN Laboratori Nazionali del Gran Sasso (LNGS), L'Aquila, Italy*
[4]*Gran Sasso Science Institute (GSSI), L'Aquila, Italy*
[5]*INFN Sezione di Roma, Roma, Italy*
[6]*Dipart. di Fisica, Sapienza Università di Roma, Roma, Italy*
[7]*Nationaal instituut voor subatomaire fysica (NIKHEF), Amsterdam, The Netherlands*
[8]*Dept. of Physics, University of Amsterdam, Amsterdam, The Netherlands*
[9]*INFN Sezione di Cagliari, Cagliari, Italy*
[10]*Dept. of Physics, Columbia University, New York, USA*
[11]*Dipart. di Scienze, Università degli Studi di Roma Tre, Roma, Italy*
[12]*INFN Sezione di Genova, Genova, Italy*
[13]*Dipart. di Fisica, Università di Genova, Genova, Italy*
[14]*Princeton University, Princeton NJ, USA*
[15]*Dipart. di Ingegneria Elettrica ed Energetica (DIEE), Sapienza Università di Roma, Roma, Italy*
[16]*Dept. of Physics, Radboud University, Nijmegen, The Netherlands*
[17]*Dipart. di Fisica, Università degli Studi dell'Aquila, L'Aquila, Italy*
[18]*Dipart. di Fisica, Università di Cagliari, Cagliari, Italy*
[19]*Dipart. di Ingegneria Astronautica, Elettrica ed Energetica, Sapienza Università di Roma, Roma, Italy*
[20]*INFN Sezione di Torino, Torino, Italy*
[21]*Dipart. di Fisica, Università di Torino, Torino, Italy*
[22]*Instituto de Fisica Corpuscular (IFIC - CSIC/UV), Paterna (Valencia), Spain*
[23]*Istituto Nazionale di Ricerca Metrologica (INRiM), Torino, Italy*
[24]*Dipart. di Elettronica & Telecomunicazioni (POLITO-ELN), Politecnico di Torino, Torino, Italy*
[25]*Dipart. Scienza Applicata e Tecnologia, Politecnico di Torino, Torino, Italy*
[26]*INFN Sezione di Napoli, Napoli, Italy*
[27]*Dipart. di Fisica, Università degli Studi di Napoli Federico II, Napoli, Italy*
[28]*INFN Sezione di Pisa, Pisa, Italy*
[29]*Dipart. di Fisica, Università di Pisa, Pisa, Italy*
[30]*Dept. of Fusion and Technology for Nuclear Safety and Security ENEA, Frascati, Italy*
[31]*Instituto de Microelectrónica de Barcelona (IMB-CNM-CSIC), Barcelona, Spain*
[32]*Dept. of Physics and Astronomy, Uppsala University, Uppsala, Sweden*
[33]*CNR-Instituto Nanoscienze, Pisa, Italy*

(Received 26 February 2026; revised 5 June 2026; accepted 14 July 2026; published 9 September 2026)

We present a study of the energy resolution of transition-edge sensors (TESs) for the detection of electrons in the 100-eV kinetic energy range. The TES is a Ti-Au bilayer with an active area of

*Contact author: benedetta.corcione@uniroma1.it

(60×60) μm^2 and a critical temperature of approximately 80 mK. The electron source is based on vertically aligned multiwall carbon nanotubes located inside the cryostat, with electrons generated via field emission. For electrons in the (92–99) eV kinetic energy range, we obtain a Gaussian energy resolution for fully absorbed electrons of $(0.48 \pm 0.04 \pm 0.06)$ eV, where the first uncertainty is statistical and the second systematic. When considering the full-width at half-maximum of the peak of the signal amplitude distribution, the corresponding resolution is of $(1.4 \pm 0.2 \pm 0.3)$ eV. The former represents an improvement of (47–60)% with respect to previous results and is mainly attributed to the reduction in the TES active area. The latter is instead an improvement of over a factor of 21 and is mainly due to the reduction in the emitting area of the electron source, which significantly suppresses electron back-scattering in proximity of the TES. These results represent a major milestone toward high-precision spectroscopy on low-energy electrons, which is a key objective for the PTOLEMY experiment.

DOI: 10.1103/dw1k-tcbp

Introduction. Transition-edge sensors (TESs) are microcalorimeters with intrinsic energy resolution capable of detecting single particles over a wide energy spectrum [1–7]. They consist of a superconductive thin film operated at the steep superconductive transition near its critical temperature T_C, where the resistance of the material is most sensitive to temperature changes [8]. When a particle hits the TES, its energy is deposited into the device via excitations of the lattice and the electronic system, leading to an increase in the TES temperature. This heating produces measurable changes in the TES resistance, which are proportional to the absorbed energy. Such detection mechanism provides the TES with an intrinsic energy resolution, making it particularly suitable to detect small energy transfers. TES devices have been extensively used as high-precision low-energy single-photon detectors, on which they have reached a Gaussian energy resolution below 50 meV for 0.8 eV photons [9,10].

Recently, TES devices have been tested for electron detection, as they offer unique possibilities compared with other devices, such as microchannel plates or silicon-based detectors. In fact, TES devices, in principle, have no dead layers and a unitary fill factor [11–13], enabling full collection and measurement of the energy deposited in the device. Moreover, the dark count rate of such devices is $\mathcal{O}$(mHz) [14], making them suitable to search for rare events; they can achieve timing resolutions of a few nanoseconds [15] and a maximum count rate of $\mathcal{O}$(mHz) [16]. These characteristics are crucial to make TES devices excellent detectors with intrinsic energy resolution, which is why this technology could play a pivotal role in low-energy electron spectroscopy [17], microcalorimetry [18,19], and experiments studying β-decay and neutrino physics [7]. Among the latter, the PTOLEMY project [20–22] plans to measure the mass of the neutrino and detect the cosmic neutrino background by analyzing the endpoint of the β^- decay spectrum of atomic tritium. To reach these objectives, the TES developed for the PTOLEMY experiment should achieve a Gaussian energy resolution of 50 meV on electrons with a kinetic energy of 10 eV. To date, a Gaussian energy resolution $\sigma_e > 17$ eV has been achieved on electrons in the 300–2000 eV energy range [17], and $0.7 < \sigma_e < 1.6$ eV on electrons with kinetic energy $91 \leq E_e \leq 101$ eV [23,24]. These latter results appear promising for the PTOLEMY application, so modifications to the experimental setup were implemented to investigate them further.

This work presents new results in which a TES device is used to measure the energy of electrons with kinetic energy in the approximately 100 eV range. Compared with the results presented in the previous work of [23], where a TES with an active area of (100×100) μm^2 and an electron source based on field emission from a 9 mm^2 carbon nanotube sample were employed, this work uses a (60×60) μm^2 TES and a 1 mm^2 carbon nanotube source. As shown below, the smaller TES improves the intrinsic energy resolution for fully absorbed electrons, while the reduced source size decreases electron back-scattering in the proximity of the TES, thereby greatly suppressing signals from electrons with sub-nominal energy. Together, these changes reduce the width of the electron energy peak by more than an order of magnitude.

Experimental setup. The measurements presented in this work are performed at the Innovative Cryogenic Laboratory of the Istituto Nazionale di Ricerca Metrologica (INRiM) in Torino (Italy). An adiabatic demagnetization refrigerator cryostat is used to maintain the TES at a stable bath temperature. Since magnetic fields affect the trajectories of electrons and the read-out system based on dc-SQUIDs [25], a magnetic shield made of Amumetal 4 K is mounted within the cryostat to surround the whole working area, which consists of the 30 mK plate hosting both the TES experimental setup and the SQUID read-out system. The shield can suppress the earth's magnetic field by a factor approximately 60.

The TES used for this work is a bilayer made of 15 nm of titanium and 30 nm of gold, with an active area of (60×60) μm^2 and a critical temperature T_C of approximately 80 mK. More details on its fabrication are reported in Ref. [23]. Its dark count rate is $\lesssim$0.8 mHz in the full energy range of the experiment of 92–99 eV, which is negligible relative to the signal rate at the selected trigger threshold, as expected from this kind of devices [14].

A sample of vertically aligned multiwall carbon nanotubes (CNTs) is used as an electron source, as they have proven to be a reliable field-emitter at cryogenic temperatures [26]. They were synthesized in the INFN laboratory 'TITAN' at Sapienza University of Rome [26–30] by chemical vapor deposition on a 500 μm silicon substrate, following the procedure described in Ref. [26], and covering an area of approximately 1 mm^2.

The CNTs are positioned in front of the TES and are voltage-biased with a negative voltage V_{CNT} to emit electrons through field emission, while the TES is electrically grounded through the cryostat and thermally connected to it. As explained in more detail in Ref. [23], to adapt the design of the TES for electron detection, a 50-nm-thick gold shield is deposited everywhere on the substrate except on the active area of the device, in order to protect both the wiring and the insulating substrate from impinging electrons, as the active area of the TES is much smaller than that of the CNTs.

According to Fowler-Nordheim theory [31], the field-emitted current increases exponentially with the applied voltage. A large electron current hitting the gold shield layer has two adverse effects: first, it causes an excessive increase in the TES temperature, which in turn decreases the TES dynamic range; secondly, some electrons are back-scattered from the gold shield layer and then enter the TES with only a fraction of their nominal energy, thus broadening their otherwise monochromatic energy spectrum. Both these aspects can be mitigated by decreasing the area of the CNT source, as fewer electrons are sent toward the device.

The kinetic energy of field-emitted electrons when they reach the TES is derived in Ref. [23] as

$$E_e = eV_{CNT} - \phi_{TES}, \tag{1}$$

where e is the elementary electric charge and ϕ_{TES} is the TES work function. The latter was measured with ultraviolet photoemission spectroscopy in the LASEC lab of Roma Tre University [26], yielding a value of $\phi_{tes} = (4.38 \pm 0.03)$ eV. Moreover, CNTs can be considered a monochromatic source, as the energy spread of the field-emitted electrons is negligible at the temperature and electric field ranges of the experiment [32]. Since field emission has an exponential dependence on the electric field, below a minimum V_{CNT} the rate of emitted electrons is too low to detect them. This defines from Eq. (1) a minimum E_e, which in our setup is $E_e^{min} \sim 92$ eV.

The TES is operated at 35% of its normal resistance $R_N \sim 0.2$ Ω, where it was found to be optimal in terms of energy resolution. To ensure stable working conditions, the TES is operated in negative electrothermal feedback, voltage-biased exploiting a shunt resistor of 20 mΩ, and the bath temperature is approximately set at half the critical temperature of the device. In series with the TES, there is a 6 nH inductance, coupled to the readout, which consists of an array of 16 dc-SQUIDs [25]. A schematic of the circuitry can be found in Ref. [23]. To guarantee a more stable voltage supply, a low-pass filter with cutoff frequency of 200 Hz is introduced on the power line of the CNTs at the 3 K stage of the cryostat, which in turn ensures a more stable field-emission current. Moreover, to reduce the high-frequency noise on the pulse shapes, the signals are preprocessed with a Moku:Lab FPGA-based unit by Liquid Instruments, using a Bessel 100 kHz low-pass filter. Since no such filter was used in the work presented in Ref. [23], we have re-processed those data by introducing an additional software-based RC low-pass filter with a cutoff frequency of 100 kHz, so as to allow for a more rigorous comparison.

Data analysis. The red histogram in Fig. 1 shows the TES signal amplitude spectrum for electrons with a kinetic energy of 96 eV and is compared with the same spectrum obtained in Ref. [23], which is shown in black in the inset. In both the distributions, the peak in the high-amplitude region is associated with events in which the electrons deposit all their energy inside the device, so it was referred

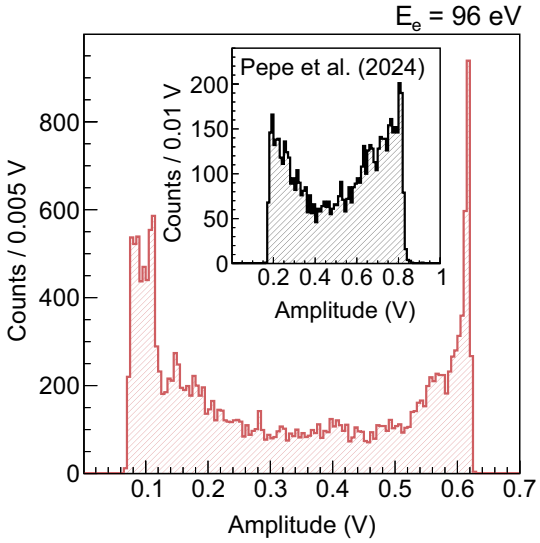

FIG. 1. Signal amplitude spectrum for 96-eV electrons (red histogram), compared with the same spectrum obtained in the previous measurement [23] (black histogram in the inset). The different amplitude scale in the two distributions is due to the fact that the red distribution refers to low-pass filtered signals, while the black distribution refers to raw pulse shapes.

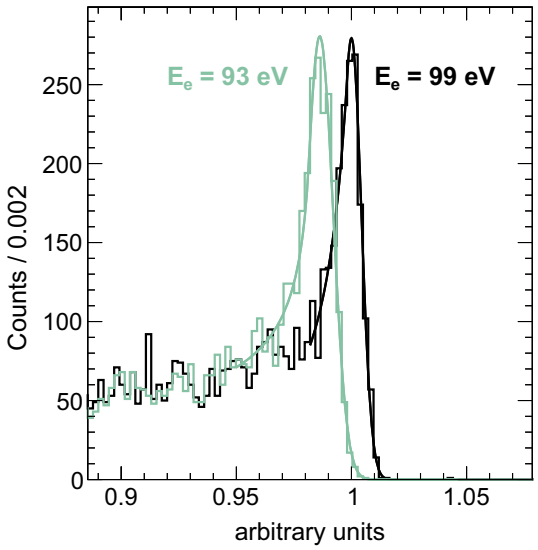

FIG. 2. Example fits of the electron absorption peaks: the green data correspond to electrons with a kinetic energy $E_e = 93$ eV, the black data to $E_e = 99$ eV. More details about the fit are given in the text.

to as "full-absorption peak." As can be seen, the tail to the left of the full-absorption peak is significantly less pronounced in the data of this work. This is mainly due to the smaller CNT sample size, which leads to fewer electrons back-scattering off the gold shield and hitting the TES active area with lower-than-nominal energy.

The absorption peaks of the distributions are fitted with a Crystal Ball function [33]: its right side with respect to the peak position (μ) is Gaussian with standard deviation σ; its left side is Gaussian up to a transition point, where it becomes a power-law tail. In particular, σ is the only parameter describing the right tail of the full-absorption peak, which is broadened by the energy resolution of the device and the energy spread of the electron source. As previously stated, the CNTs in our working conditions emit monochromatic electrons, so σ is dominated by the energy resolution of the device. The power-law tail instead describes partially absorbed electrons. The full-absorption peak is fitted in a range between $\pm 2\%$ with respect to the peak position. Figure 2 shows two typical fits to the absorption peaks: the data corresponding to electrons with a kinetic energy of 93 (99) eV are shown in green (black). As for the data presented in Ref. [23] and postfiltered, they are fitted with an asymmetric Gaussian function, as explained in the previous work.

The electron energy resolution is defined using both σ and the full-width at half-maximum (FWHM), respectively, as $\Delta E_{\mathrm{gaus}} = (\sigma/\mu) \times E_e$ and $\Delta E_{\mathrm{fwhm}} = (\mathrm{FWHM}/\mu) \times E_e$, where the electron kinetic energy E_e is defined in Eq. (1). The FWHM is obtained directly from the histogram of signal amplitude. Figure 3 shows the energy resolutions ΔE_{gaus} and ΔE_{fwhm} achieved by this work (blue squares). These are in turn compared with the

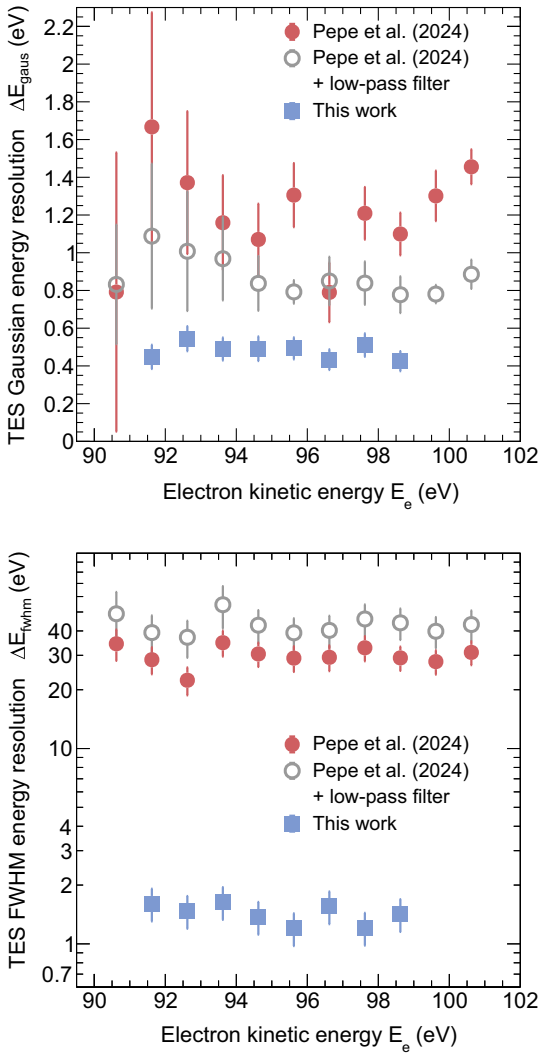

FIG. 3. Top: TES Gaussian energy resolution ΔE_{gaus} for electrons, as a function of their kinetic energy E_e. Bottom: TES full-width at half-maximum energy resolution ΔE_{fwhm} for electrons, as a function of their kinetic energy E_e, with logarithmic scale on the y axis.

data recorded in Ref. [23], both in their original form (full red circles) and after the application of a 100 kHz low-pass filter (open gray circles). These results are also summarized in Table I.

As discussed in the experimental setup section, the data reported in Ref. [23] were re-processed using a low-pass filter matched to the signal conditioning employed in the present work, in order to enable a consistent comparison. Under these conditions, the re-processed dataset exhibits an improvement of approximately 26% in ΔE_{gaus} with respect to the raw data. Using the present setup, we obtain a Gaussian energy resolution of $\langle \Delta E_{\mathrm{gaus}} \rangle = (0.48 \pm 0.04 \pm 0.06)$ eV, where the average has been made across the full energy range, and the first uncertainty is statistical and the second is systematic. This corresponds to a 60% (46%) improvement over the raw (filtered) data

TABLE I. Summary of TES energy resolution results. The values reported in the last two columns correspond, respectively, to the average ΔE_{gaus} and ΔE_{fwhm} values obtained on the studied electron energy range. Uncertainties are statistical in nature.

Dataset	TES area (μm^2)	CNT area (mm^2)	E_e (eV)	$\langle \Delta E_{\mathrm{gaus}} \rangle$ (eV)	$\langle \Delta E_{\mathrm{fwhm}} \rangle$ (eV)
Pepe *et al.* [23](raw)	100×100	9	91–101	1.2 ± 0.3	30 ± 4
Pepe *et al.* [23](low-pass filter)	100×100	9	91–101	0.9 ± 0.1	43 ± 5
This work	60×60	1	92–99	0.48 ± 0.04	1.4 ± 0.2

of our previous work. The improvement with respect to the filtered data is roughly in line with the expected approximately 40% improvement in TES energy resolution coming from the reduction in the TES active area. In fact, the intrinsic energy resolution of a TES is known to be proportional to the square root of its active area: in fact, the intrinsic energy resolution of a TES is known to scale with the square root of its heat capacity, which in turn depends on the TES volume [8]. Therefore, keeping the film thickness constant, reducing the TES active area lowers its heat capacity and results in a larger temperature rise for the same absorbed energy, ultimately improving the detector response and energy resolution. These results indicate that the observed performance enhancement in the present work is primarily driven by detector design rather than by differences in signal filtering.

The FWHM of the absorption peak, on the other hand, is strongly influenced by the reduced size of the CNT emitting area. As shown in Fig. 3 bottom, we obtain, when averaging across the full electron energy range, $\langle \Delta E_{\mathrm{fwhm}} \rangle = (1.4 \pm 0.2 \pm 0.3)$ eV. This corresponds to an improvement of a factor 21 (31) with respect to the raw (filtered) data of our previous work. It is worth noting that, differently from the case of ΔE_{gaus}, in this case the resolution of our previous setup is worsened by the application of the low-pass filter. In fact, while the width of the right tail of the absorption peak is mainly driven by statistical resolution effects and therefore benefits from filtering, its left tail, in the case of [23], is largely dominated by unwanted signals of partially absorbed electrons that persist even after filtering, whose amplitude distribution is modified by the effect of the filter and happens to lead to a wider left tail, and consequently to a worse ΔE_{fwhm}.

The main systematic uncertainty concerns the choice of the fitting model. To estimate this, the systematic uncertainty of the ΔE_{gaus} is calculated by evaluating the variation in energy resolution obtained by using an asymmetric Gaussian instead of a Crystal Ball. This results in a value of 12% for the data of this work, determined as the difference in ΔE_{gaus} obtained with the two different functions, averaged across the tested electron energies. To estimate the systematic uncertainty on ΔE_{fwhm}, the FWHM derived directly from the distribution of the data is compared with the FWHM analytically calculated from the parameters of the fit. The resulting systematic uncertainties are 19%, 14%, and 18% for the new data, the previous data, and the previous data postfiltered, respectively, all averaged on the different applied voltages. Moreover, to validate all the results obtained fitting the histograms, the effect of different binnings and fitting ranges is studied. The discrepancy among different energy resolution results is approximately 3%, which is added in quadrature to the other sources of uncertainty. The total uncertainty reported in the error bars of Fig. 3 represents the quadrature sum of the statistical contribution and the systematic contribution. The ΔE_{gaus} of the data already presented in Ref. [23] (full red circles) is shown as originally published, and to allow for a more rigorous comparison, no additional uncertainty is added to the corresponding filtered dataset (open gray circles), to which the same uncertainties reported in Ref. [23] are applied.

In addition to improving the TES energy resolution, reducing the emitting surface of the electron source mitigates the heating effect associated with field emission observed in Ref. [23]. This aspect is illustrated in Fig. 4, where the values of Joule power P_J required to bring the TES to its working point on the superconductive transition

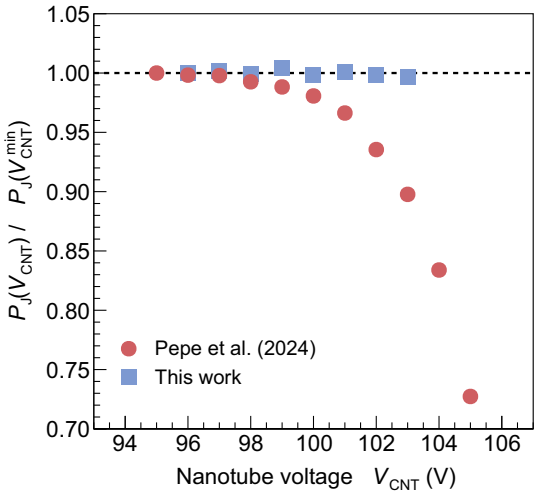

FIG. 4. Joule power P_J needed to bring the TES to its working point for different values of V_{CNT}, normalized to the Joule power needed for the lowest V_{CNT} value. A black dashed line corresponding to unity is plotted to guide the eye.

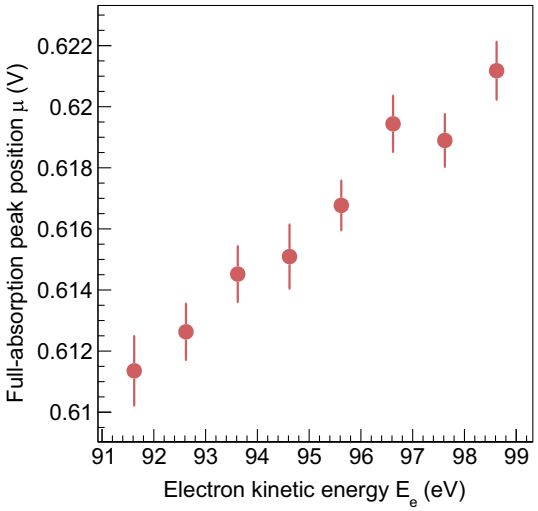

FIG. 5. Full-absorption peak position μ as a function of electron kinetic energy E_e.

are plotted with respect to the applied bias voltage V_{CNT}. In order to compare different measurements, each dataset is normalized to the Joule power dissipated at the lowest V_{CNT} analyzed. As can be seen, in the data of this work (blue squares) no relevant heating is present, as the Joule power needed to polarize the TES at its operating temperature remains stable. In the previous data (red circular markers), instead, an exponential reduction in the Joule power P_J dissipated through the TES with increasing V_{CNT} can be observed, indicating a corresponding increase in the substrate temperature. Operating the TES under consistent conditions ensures that measurements performed at different V_{CNT} values, corresponding to different electron kinetic energies, can be rigorously compared without applying additional corrections. We have furthermore verified that the peak position μ of the Crystal Ball fit function increases linearly with V_{CNT}, confirming the stability of the TES working conditions, as can be appreciated in Fig. 5.

Conclusions. We have presented a new experimental setup for the PTOLEMY experiment to investigate the energy resolution of a TES characterized with monochromatic electrons in the 100-eV kinetic energy range. Compared with our previous work [23], we have employed a TES with a smaller active area of (60×60) μm^2, and a smaller electron source, based on field emission from a (1×1) mm^2 chip of vertically aligned carbon nanotubes (CNTs). We report a remarkable improvement in the energy resolution, both in the Gaussian width of the full-absorption peak (ΔE_{gaus}), and in the full-width at half-maximum broadness of the peak (ΔE_{fwhm}). When averaging the results over the full energy range, we obtain $\langle \Delta E_{gaus} \rangle = (0.48 \pm 0.04 \pm 0.06)$ eV, which corresponds to a 60% improvement with respect to the raw data of our previous work, and to a 47% improvement with respect to that same data after the application of a low-pass filter with a frequency of 100 kHz. This improvement is in line with the expectations deriving from the reduction of the TES active area. Taking the same average on ΔE_{fwhm} yields $\langle \Delta E_{fwhm} \rangle = (1.4 \pm 0.2 \pm 0.3)$ eV, which corresponds to an improvement of a factor 21 (31) with respect to the raw (filtered) data of our previous work. This large improvement, of over an order of magnitude, is mainly due to the reduction in the CNT source size and represents a major step forward in the spectroscopy of low-energy electrons.

To keep testing the potential of TES devices with electrons, lower energies will be tested by inserting a decelerating plate inside the experimental setup. This will allow us to reach the energy range $E_e \sim 10$ eV required by the PTOLEMY collaboration, further decreasing the size of the TES detectors to improve their intrinsic energy resolution. Since the devices will be smaller, a larger amount of them will be required to geometrically cover the full spatial distribution of electrons at the end of the PTOLEMY filter, resulting in an array of TESs. Consequently, the total rate of electrons originating from the tritium source will be distributed across the entire TES array rather than concentrated on an individual device.

Acknowledgments. The authors are grateful to Elio Bertacco, Martina Marzano, Matteo Fretto, and Ivan De Carlo for technical support. This research was partially funded by the contribution of Grant No. 62313 from the John Templeton Foundation, by PRIN grant "ANDROMeDa" (PRIN 2020Y2JMP5) and PRIN grant "TES4e" (PRIN 2022 202285H5MT) of Ministero dell'Università e della Ricerca, and from the EC project ATTRACT (Grant Agreement No. 777222). We also acknowledge funding from the Agencia Estatal de Investigacion (Ref. CNS2023-145234).

Data availability. The data that support the findings of this article are openly available at https://doi.org/10.5281/zenodo.18786228, as reported in the citation [34] of the paper, embargo periods may apply.

[1] J. M. Gildemeister, A. T. Lee, and P. L. Richards, A fully lithographed voltage-biased superconducting spiderweb bolometer, Appl. Phys. Lett. **74**, 868 (1999).
[2] K. Irwin, An application of electrothermal feedback for high resolution cryogenic particle detection, Appl. Phys. Lett. **66**, 1998 (1995).
[3] B. Cabrera, R. M. Clarke, P. Colling, A. J. Miller, S. Nam, and R. W. Romani, Detection of single infrared, optical, and ultraviolet photons using superconducting transition edge sensors, Appl. Phys. Lett. **73**, 735 (1998).
[4] D. T. Chow, A. Loshak, M. L. van den Berg, M. A. Frank, T. W. Barbee, Jr., and S. E. Labov, High-resolution gamma-ray spectrometers using bulk absorbers coupled to Mo/Cu

multilayer superconducting transition-edge sensors, in *Hard X-ray, Gamma-Ray, and Neutron Detector Physics II* (SPIE, Bellingham, WA, USA, 2000), Vol. 4141, pp. 67–75.

[5] G. Angloher, P. Bauer, N. Ferreiro, D. Hauff, A. Tanzke, R. Strauss, M. Kiefer, F. Petricia, F. Reindl, W. Seidel *et al.*, Quasiparticle diffusion in Cresst light detectors, J. Low Temp. Phys. **184**, 323 (2016).

[6] T. Saab, R. M. Clarke, B. Cabrera, R. A. Abusaidi, and R. Gaitskell, Design of QET phonon sensors for the CDMS ZIP detectors, Nucl. Instrum. Methods Phys. Res., Sect. A **444**, 300 (2000).

[7] A. Orlando, V. Ceriale, G. Ceruti, M. De Gerone, M. Faverzani, E. Ferri, G. Gallucci, A. Giachero, A. Nucciotti, A. Puiu *et al.*, Microfabrication of transition-edge sensor arrays of microcalorimeters with ^{163}Ho for direct neutrino mass measurements with HOLMES, J. Low Temp. Phys. **193**, 771 (2018).

[8] K. D. Irwin and G. C. Hilton, Transition-edge sensors, in *Cryogenic Particle Detection* (Springer, New York, 2005), pp. 63–150.

[9] L. Lolli, E. Taralli, C. Portesi, E. Monticone, and M. Rajteri, High intrinsic energy resolution photon number resolving detectors, Appl. Phys. Lett. **103**, 041107 (2013).

[10] K. Hattori, T. Konno, Y. Miura, S. Takasu, and D. Fukuda, An optical transition-edge sensor with high energy resolution, Supercond. Sci. Technol. **35**, 095002 (2022).

[11] A. Apponi, F. Pandolfi, I. Rago, G. Cavoto, C. Mariani, and A. Ruocco, Absolute efficiency of a two-stage microchannel plate for electrons in the 30–900 eV energy range, Meas. Sci. Technol. **33**, 025102 (2021).

[12] A. Apponi, G. Cavoto, M. Iannone, C. Mariani, F. Pandolfi, D. Paoloni, I. Rago, and A. Ruocco, Response of windowless silicon avalanche photo-diodes to electrons in the 90–900 eV range, J. Instrum. **15**, P11015 (2020).

[13] M. Gugiatti, M. Biassoni, M. Carminati, O. Cremonesi, C. Fiorini, P. King, P. Lechner, S. Mertens, L. Pagnanini, M. Pavan *et al.*, Characterisation of a silicon drift detector for high-resolution electron spectroscopy, Nucl. Instrum. Methods Phys. Res., Sect. A **979**, 164474 (2020).

[14] L. Manenti, C. Pepe, I. Sarnoff, T. Ibrayev, P. Oikonomou, A. Knyazev, E. Monticone, H. Garrone, F. Alder, O. Fawwaz *et al.*, Dark counts in optical superconducting transition-edge sensors for rare-event searches, Phys. Rev. Appl. **22**, 024051 (2024).

[15] A. Lamas-Linares, B. Calkins, N. A. Tomlin, T. Gerrits, A. E. Lita, J. Beyer, R. P. Mirin, and S. Woo Nam, Nanosecond-scale timing jitter for single photon detection in transition edge sensors, Appl. Phys. Lett. **102**, 231117 (2013).

[16] R. Kobayashi, K. Hattori, S. Inoue, and D. Fukuda, Development of a fast response titanium-gold bilayer optical TES with an optical fiber self-alignment structure, IEEE Trans. Appl. Supercond. **29**, 1 (2019).

[17] K. M. Patel, S. Withington, A. G. Shard, D. J. Goldie, and C. N. Thomas, Electron spectroscopy using transition-edge sensors, J. Appl. Phys. **135**, 224504 (2024).

[18] M. Loidl, J. Beyer, L. Bockhorn, C. Enss, S. Kempf, K. Kossert, R. Mariam, O. Nähle, M. Paulsen, P. Ranitzsch *et al.*, Beta spectrometry with metallic magnetic calorimeters in the framework of the European EMPIR project MetroBeta, Appl. Radiat. Isot. **153**, 108830 (2019).

[19] R. P. Fitzgerald, B. K. Alpert, D. T. Becker, D. E. Bergeron, R. M. Essex, K. Morgan, S. Nour, G. O'Neil, D. R. Schmidt, G. A. Shaw *et al.*, Toward a new primary standardization of radionuclide massic activity using microcalorimetry and quantitative milligram-scale samples, J. Res. Natl. Inst. Stand. Technol. **126**, 126048 (2022).

[20] M. Betti, M. Biasotti, A. Boscá, F. Calle, J. Carabe-Lopez, G. Cavoto, C. Chang, W. Chung, A. Cocco, A. Colijn *et al.*, A design for an electromagnetic filter for precision energy measurements at the tritium endpoint, Prog. Part. Nucl. Phys. **106**, 120 (2019).

[21] M. Betti, M. Biasotti, A. Boscá, F. Calle, N. Canci, G. Cavoto, C. Chang, A. Cocco, A. Colijn, J. Conrad *et al.*, Neutrino physics with the PTOLEMY project: Active neutrino properties and the light sterile case, J. Cosmol. Astropart. Phys. 2019, 047 (2009).

[22] A. Apponi, M. Betti, M. Borghesi, N. Canci, G. Cavoto, C. Chang, W. Chung, A. Cocco, A. Colijn, N. D'Ambrosio *et al.*, Implementation and optimization of the PTOLEMY transverse drift electromagnetic filter, J. Instrum. **17**, P05021 (2022).

[23] C. Pepe, B. Corcione, F. Pandolfi, H. Garrone, E. Monticone, I. Rago, G. Cavoto, A. Apponi, A. Ruocco, F. Malnati *et al.*, Detection of low-energy electrons with transition-edge sensors, Phys. Rev. Appl. **22**, L041007 (2024).

[24] B. Corcione, Detection of low-energy electrons with transition-edge sensors, Il Nuovo Cimento C **48**, 187 (2025).

[25] D. Drung, C. Assmann, J. Beyer, A. Kirste, M. Peters, F. Ruede, and T. Schurig, Highly sensitive and easy-to-use squid sensors, IEEE Trans. Appl. Supercond. **17**, 699 (2007).

[26] L. Cecchini, C. Pepe, B. Corcione, O. Castellano, D. Paoloni, F. Malnati, G. Cavoto, M. Carminati, C. Fiorini, G. Pettinari *et al.*, Quantitative correlation between carbon nanotube tip morphology and field emission properties at cryogenic temperature, Nanoscale **17**, 21260 (2025).

[27] E. Schifano, G. Cavoto, F. Pandolfi, G. Pettinari, A. Apponi, A. Ruocco, D. Uccelletti, and I. Rago, Plasma-etched vertically aligned CNTs with enhanced antibacterial power, Nanomaterials **13**, 1081 (2023).

[28] R. P. Yadav, I. Rago, F. Pandolfi, C. Mariani, A. Ruocco, S. Tayyab, A. Apponi, and G. Cavoto, Evaluation of vertical alignment in carbon nanotubes: A quantitative approach, Nucl. Instrum. Methods Phys. Res., Sect. A **1060**, 169081 (2024).

[29] F. Sarasini, J. Tirillò, M. Lilli, M. P. Bracciale, P. E. Vullum, F. Berto, G. De Bellis, A. Tamburrano, G. Cavoto, F. Pandolfi *et al.*, Highly aligned growth of carbon nanotube forests with in-situ catalyst generation: A route to multifunctional basalt fibres, Composites, Part B **243**, 110136 (2022).

[30] S. Tayyab, A. Apponi, M. G. Betti, E. Blundo, G. Cavoto, R. Frisenda, N. Jiménez-Arévalo, C. Mariani, F. Pandolfi, A. Polimeni *et al.*, Spectromicroscopy study of induced defects in ion-bombarded highly aligned carbon nanotubes, Nanomaterials **14**, 77 (2023).

[31] R. H. Fowler and L. Nordheim, Electron emission in intense electric fields, Proc. R. Soc. London, Ser. A **119**, 173 (1928).

[32] R. Gomer, Field emission, field ionization, and field desorption, Surf. Sci. **299–300**, 129 (1994).

[33] M. J. Oreglia, Study of the reactions $\psi' \to \gamma\gamma\psi$ [Thesis], Tech. Rep., SLAC National Accelerator Laboratory (SLAC), Menlo Park, CA (United States), 1980.

[34] Shared data for this paper: https://zenodo.org/records/18786228.